An In Situ and Real Time Plasmonic Approach of Seed/Adhesion Layers: Chromium Buer Eect at the Zinc/Alumina Interface

Maya Messaykeh, Stéphane Chenot, Pascal David, Gregory Cabailh, Jacques Jupille, Alexey Koltsov, Remi Lazzari

An *In Situ* and Real Time Plasmonic Approach of Seed/Adhesion Layers: Chromium Buffer Effect at the Zinc/Alumina Interface

Maya Messaykeh,[†] Stéphane Chenot,[†] Pascal David,[†] Gregory Cabailh,[†] Jacques Jupille,[†] Alexey Koltsov,[‡] and Rémi Lazzari*,[†]

[†]*CNRS, Sorbonne Université, Institut des NanoSciences de Paris, UMR 7588, 4 Place Jussieu, F-75005 Paris, France*

[‡]*ArcelorMittal Maizières Research, voie Romaine, F-57280, Maizières-lès-Metz, France*

E-mail: remi.lazzari@insp.jussieu.fr

Abstract

The effect of additives on metal/oxide interfaces is explored *in situ* and in real time on evaporated films by a combination of surface science techniques, among which a very flexible optical method shows a unique ability to scrutinize the growth and wetting properties of supported clusters that involve several elements. The study focuses on Cr at the Zn/α-Al_2O_3(0001) interface at 300 K. A particular interest of the present interface is that Zn does not stick at all on bare alumina. The sticking and morphology of both Cr and Zn films are analyzed from submonolayer to multilayer thicknesses, during their growth. After an initial oxidation reaction with residual OH groups, shown to be detrimental to Zn adhesion, Cr growth proceeds through the formation of high aspect ratio particles that percolate around an average thickness of 10 Å. As regards to Zn growth on a Cr deposit, two very distinct stages can be distinguished. In the submonolayer thickness range, Cr forms a seed layer that drastically increases the Zn sticking coefficient from zero to nearly one due to a diffusion length of physisorbed Zn adatoms before desorption larger than Cr island separation; Zn clusters are anchored on the Cr seeds that they encapsulate, but their wetting behavior is dictated by the interaction with alumina. In a second stage, as soon as the Cr film percolates, it forms an adhesion layer on which Zn grows in a nearly 2D mode. In all cases, Cr films are stable upon annealing. On Cr-covered alumina, the Zn desorption energy is enhanced as compared to bare surfaces which, in line with atomistic simulations, is assigned to the formation of more favorable Cr-Al_2O_3 and Cr-Zn than Zn-Al_2O_3 bonds. Generally speaking, the ability demonstrated herein of small amounts of additives to dramatically increase the adhesion of films is of great practical interest. It shows that non-continuous and partially oxidized films of additives, closer to realistic cases of application, can strongly enhance the sticking of films. Also, anchoring a functional film by discrete pre-deposited seeds can keep its properties intact.

1 Introduction

Oxide-supported continuous metallic films are involved in countless fields.[1] A constant obstacle to their applications is the poor wetting of dielectric substrates by metals[2,3] which leads to 3D growth morphology, in particular in the case of late transition or coinage metals (Cu, Zn, Ag, Pt, Au) when these are often the most relevant choices for their specific properties. Kinetics can compensate for thermodynam-

ics and allows percolation by acting on the atom diffusion lengths via the substrate temperature, the flux of impinging species or even their kinetic energy. Yet synthesized films are inherently out-of-equilibrium and prone to mechanical failure due to stress,[4,5] aging or dewetting[6–8] that are detrimental to the continuous film properties. Therefore, obtaining reliable assemblies requires more sophisticated engineering solutions, such as the pre-deposited intermediate layers used to stabilize transparent conductive films, metamaterials or plasmonics devices which need flat and sharp interfaces as well as optimized thickness[9] and roughness.[10,11,11–15] Those layers are called alternatively seed[10,12,13,16] or nucleation[14] layers, adhesion[17–19] or wetting[11] layers, surfactants,[9,20] or buffers.[21,22] The term "buffer" will be used in what follows, because of its generality, before more precise indications emerge from the discussion. Buffers commonly involve transition metals (Ni;[23] Cr,Ti;[9,16–19,22,24] Nb;[10] Ta;[16] Zr;[16] W[16]), Sn,[20] Cu,[13] Ge[11,12,14] or even some specific oxides.[17,18]

From a thermodynamic adhesion point of view, buffers replace the weak metal/substrate bonds by stronger metal/metal and metal/substrate bonds that basically scale with the heat of formation of the parent metal oxides.[25–27] But, according to the Bauer criterion,[28] this favorable effect is balanced by the intrinsic non-wetting behavior of transition metals used in buffers on oxides such as alumina and silica.[29,30] However in practice, from a growth point of view, they spread quite well because of a reduced surface mobility as often pointed by their low homologous (growth/melting) temperatures.[28,31,32] Images recorded *ex situ* by atomic force microscopy (AFM) in Figure 1 illustrate the point. Silver deposited on alumina at 300 K forms 3D aggregates (Figure 1-a) close to equilibrium since the found contact angle (127°)[22,33,34] is equal to that measured by the sessile drop method (127 − 131°).[25,29] In the case of titanium, the "contact angle" determined at 300 K (∼ 30°),[22,35] although much smaller than the equilibrium value (78°),[25,29] clearly shows that the metal does not perfectly wet the oxide. However, because the apparent growth mode is largely based on kinetics, Ti quickly covers the surface unlike Ag (Figure 1-b versus 1-a). Similar AFM images are observed for Al/[22] and Co/alumina,[36] although these metals do not wet this oxide from a thermodynamic point of view.[29] Generally speaking, the highly electropositive metals used in buffers to enhance the adhesion of late transition and coinage metals do no wet large band gap oxides such as alumina and silica.[29,30] These contrasting behaviors are central in buffer effects.

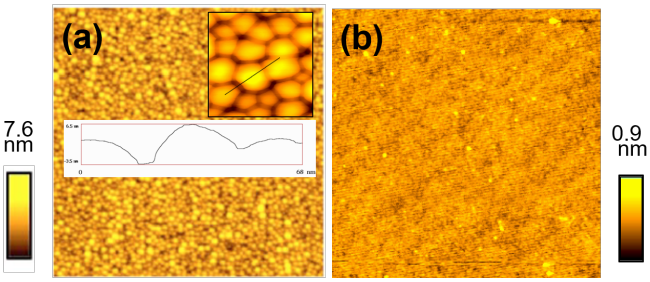

Figure 1: Atomic force microscopy images (1×1) μm^2 recorded *ex situ* of metal/α-Al_2O_3(0001) films deposited in ultra-high vacuum at 300 K: (a) 3 nm Ag (from Reference 22); the inset shows a (100×100) nm zoom with the height profile corresponding to the black line; (b) 1.4 nm Ti; the steps of the alumina surface are visible with heights corresponding to interatomic distances (from Reference 35).

Most studies focus on final effects of rather thick (> 1 nm) buffer layers but neglect *in situ* observation of the growth and interfacial chemistry despite the importance of the morphology of buffers on how they operate. For example, the reduction in thickness of buffers is frequently sought to minimize their impact on the properties of coatings,[9,10,12,18,20] although the behavior of these additives in the submonolayer range can be suspected to differ greatly from that of thicker layers, whose effects, far from uniform,[16] can even become detrimental.[16,21] The present work aims to monitor *in situ* and in real time, by surface differential reflectivity spectroscopy, the mechanisms involved from the very first stages of the growth of Zn on Cr-precovered alumina surfaces. The case is

relevant to the development of advanced high-strength steels (AHSS) used by the automotive industry to lighten car weight to comply with energy saving rules. To improve mechanical properties, AHSS grades involve electropositive elements such as Al whose drawback is the oxygen-induced segregation at steel surfaces.[37–39] The resulting surface oxide then degrades the adhesion of the anti-corrosive Zn coating during the galvanization process.[40,41] The issue has motivated a series of studies[42–47] on the model Zn/α-Al_2O_3(0001) interface. First-principle simulations[43,44,46] have shown the effectiveness of Cr > Fe > Ni in promoting strong metal-oxygen and metal-zinc bonds and shifting cleavage from interfacial to cohesive. In a surface science perspective, the effect of the Cr additive on the Zn/Cr/α-Al_2O_3(0001) adhesion offers a unique test bed since, under ultra-high vacuum (UHV), Zn does not stick at all on bare alumina above 220 K.[45,48,49] Moreover, the α-Al_2O_3(0001) surface is a popular support[10,21,22,24,26] and Cr is a common additive[9,16–18] which is theoretically predicted to be highly efficient at the Zn/α-Al_2O_3(0001) interface.[46]

The used differential reflectivity technique has proven its ability to analyze growing films of Ag,[22,33,34] Al,[22] Ti[22] and Zn[45] at coverages of a tenth of a monolayer or less. The direct determination of the aspect ratio of supported particles allows an unique approach of their wetting.[22,33,34,45,50] The interplay between the pre-deposited Cr buffer and the sticking and adhesion of the Zn overlayer is explored herein by an *in situ* approach performed in UHV conditions from the very early stages of the film growth. In addition, the study implements photoemission spectroscopy to determine chemical state and thickness but also temperature programmed desorption to probe Zn bonding. The question at hand is the role of Cr film thickness, chemical state and morphology in the improvement of Zn sticking and adhesion.

2 Experimental details

Experiments have been performed in a UHV vessel composed of a preparation (base pressure 2.10^{-10} mbar) and an analysis chamber (5.10^{-11} mbar) equipped with X-ray Photoelectron Spectroscopy (XPS), Low Energy Electron Diffraction (LEED), Temperature Programmed Desorption (TPD) and Surface Differential Reflectivity Spectroscopy (SDRS). Epipolished ($9 \times 9 \times 0.5$) mm^3 α-Al_2O_3(0001) single crystals (supplier MaTecK[51]) were annealed at $\sim$ 1200 K by electron bombardment of the sample backplate under pure grade oxygen; gas was provided by a carefully out-gased doser, made of a bundle of metallic tubes, placed a millimeter from the surface to increase the local partial pressure by more than an order of magnitude compared to the chamber pressure ($p \simeq 2.10^{-6}$ mbar).[52] A sharp (1×1) LEED pattern was then obtained. Al-rich reconstructed surfaces [$(\sqrt{3} \times \sqrt{3})$R30°, $(3\sqrt{3} \times 3\sqrt{3})$R30° or $(\sqrt{31} \times \sqrt{31})$R $\pm$ 9°] obtained by high temperature annealing in vacuum[53–55] have served as models of dry (or OH free) surface in TPD.[45] Contaminants, in particular carbon, were below the detection limit of XPS, except for calcium that segregated up to an apparent thickness of 1 Å on reconstructed surfaces. It does not impact LEED nor X-ray[53–55] patterns, *i.e.* the surface crystallography. Previous transmission electron microscopy[56] pointed to a Ca spread over four subsurface cation planes. Because of these observations and since Ca, absent from the environment of Cr probed by Extended X-ray Absorption Fine Structure,[47] does not show XPS change upon Cr deposition, it has been assumed not to affect the following conclusions.

Cr was evaporated from a metallic rod heated by electron bombardment (Omicron EFM3) and Zn from an effusion cell (MBE Komponenten) held at 643 K. Both sources were calibrated by a quartz microbalance set at the sample location (evaporation rate $\sim$ 1 Å.min^{-1}). However, thicknesses used herein refer only to photoemission determination (see below). Depositions were performed at 300 K at a base

pressure $p < 1.10^{-9}$ mbar. Although no significant metallic Cr aging was observed over the time scale of measurements, no cumulative deposition was performed. A new substrate was used for each Cr deposit. Cr oxide layers were obtained by prolonged oxidation at $T \sim 1575$ K of Cr films under gas doser ($p = 2.10^{-6}$ mbar); thicknesses were determined by photoemission assuming a Cr_2O_3 structure. Cr and Zn growths were followed in real time by SDRS in the ultra-violet/visible photon range (1.5-5.5 eV) both in p- and s-polarizations.[57] Spectra were systematically normalized to the bare alumina reflectivity. The reflection coefficients of the films were expressed using interfacial susceptibilities that have the meaning of "dielectric thicknesses" which combine geometry and dielectric properties (see References 58,59 for definitions). By polarizing metal particles, the electric field of the incident light (incidence of $\theta_0 = 45°$) excites plasmon resonances which are sensitive to morphology even for transition metals, despite broadening.[50,57] To derive particle shape from optics, islands were modeled by truncated spheroids[35] to fit recorded spectra in the framework of a dielectric formalism[22,33,57,60] (Section SII of supporting information). These are in line with previous dielectric simulations[57,61–65] which turned out to be efficient in unraveling growth modes and change in wetting[22,33,50,60] at metal/dielectric interfaces. For both Cr and Zn films, only s-polarization has been considered since, beyond a scaling in intensity due to substrate reflectivity, the response for the two polarizations hardly differs for flat particles (Figures S1-b,c, S2, S3 and S4).

Chemical states and thicknesses were examined by XPS at normal emission under non-monochromatic excitation with a hemispherical analyzer (Phoibos 100 from SPECS; delay line detector) at a pass energy of either 20 eV or 50 eV. Al-Kα and Mg-Kα excitations were used alternatively for Cr and Cr+Zn deposits to avoid overlap between core levels and Auger transitions. No charge compensation was applied. Ratios of substrate (O 1s and Al 2s) and deposit (Cr 2p and Zn 2p) core-level areas were used to estimate thicknesses after correction from analyzer transmission function and photoionization cross sections[66] (Table S1). Areas were obtained after subtraction of a Tougaard universal background[67] with parameters $B = 3006$ eV^2 and $C = 1643$ eV^2. Care was taken to subtract the second plasmon satellite of O 1s under the Cr 2p core level to quantify thin Cr films. Despite partial coverage, a model of signal damping through a stack of continuous films[68] was used with effective attenuation lengths (Table S2) obtained by combining elastic transport theory[69–71] and TPP2M predictive formula[72] for inelastic mean free paths as implemented in the *I4P* package.[73] Bulk densities and stoichiometries of Cr, Zn and Cr_2O_3 were used to define film thicknesses.

Zn desorption (mass/charge of $m/e = 64$) was followed by TPD from 300 to 700 K at a heating rate of 0.33 K.s^{-1}. The mass spectrometer (MS, PrismaPlus QMG220) was enclosed in a quartz tube the aperture of which was brought in the vicinity of the substrate (in such way that the sample is in line of sight of the MS) to only probe Zn desorption.[45] Desorption energy and order were obtained from the Polanyi-Wigner equation[74] using the Redhead formula[75] or the leading edge analysis[76] (see supplemental material of Reference 45 and Section SIII).

3 Results and discussion

To explore the impact of Cr buffers on the sticking and adhesion of Zn, alumina substrates precovered by increasing amounts of Cr were exposed to a given Zn dose of $\sim$ 15 Å. Similar deposits were also performed on purposely oxidized Cr films. The growth of Cr/α-Al_2O_3(0001), the sticking, desorption and growth of Zn deposited on Cr/α-Al_2O_3(0001) are successively presented.

3.1 Chromium growth mode on α-Al_2O_3(0001) from optics

The growth of Cr/Al_2O_3(0001) was monitored by SDRS (Figure 2-a,b). The similarity between the dielectric constants of Cr (Figure S1-

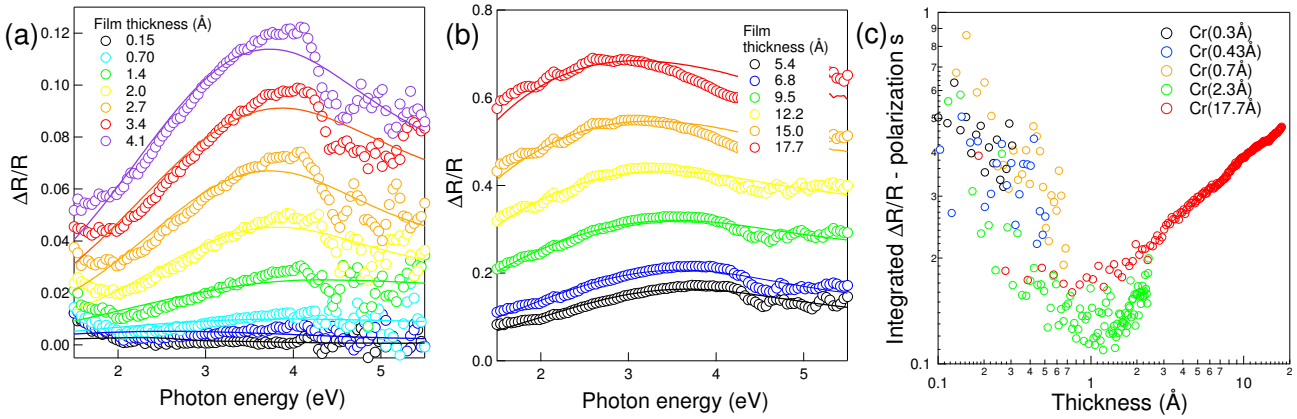

Figure 2: Differential reflectivity during growth of $Cr/Al_2O_3(0001)$: (a)(b) fits (lines) with a dielectric model of the s-polarization spectra (points). Film thicknesses are scaled on evaporation time from the obtained photoemission calibration at the end of the deposition process. The higher noise in the ultraviolet range is due to a lower absolute reference signal. (c) Evolution with thickness of the integrated SDRS s-polarized signal $\mathcal{A}_s$ normalized to thickness (Equation 1) for different Cr deposits. Integration is performed over the accessible photon energy range.

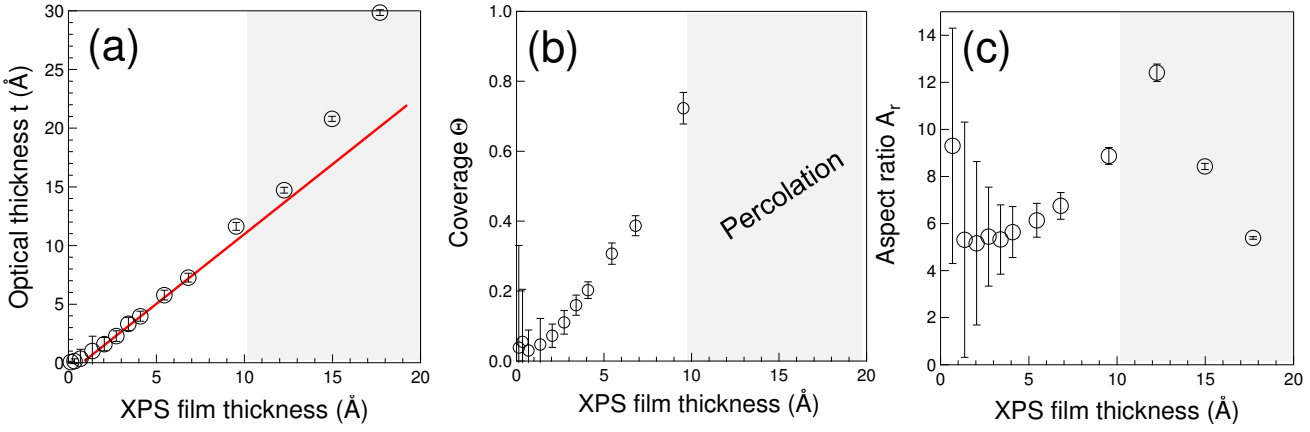

Figure 3: Morphology of $Cr/Al_2O_3(0001)$ from SDRS fits: (a) optical thickness t, (b) surface coverage Θ and (c) particle aspect ratio A_r versus deposited thickness. Shaded regions correspond to the breakdown of the model with hemispheroids, which is associated to the percolation within the Cr film.

a) and Zn (Figure S4-a) combined with previous findings on plasmonics of Zn/Al_2O_3[59] shows that the observed broad resonance for Cr corresponds to the excitation in particles of a parallel dipole polarization mode on the tail of interband transitions.[77] The evolution of the particle aspect ratio (A_r=parallel diameter/height) and therefore wetting can be gained through the integrated SDRS signal in s-polarization, normalized to film thickness t,[50] defined by:

$$\mathcal{A}_s(t) = \frac{c}{4\cos\theta_0 t(\epsilon_S - 1)} \int_0^\infty \frac{\Delta R_s}{R_s}(\omega, t)\frac{d\omega}{\omega} \quad (1)$$

where ϵ_S is the dielectric function of alumina ($\epsilon_S \simeq 3$ in ultra-violet/visible), θ_0 the incident angle and c the speed of light. Mainly driven by the oscillator strength of the parallel plasmon resonance, $\mathcal{A}_s(t)$ directly accounts for A_r.[50] Its reproducible U-shaped evolution (Figure 2-c) points to a 3D growth mode with (i) an initial stress-driven flattening ($t < 1$ Å), (ii) a growth at constant A_r around $t \simeq 1$ Å and (iii) a coalescence/coarsening ($t > 2$ Å)[50] that occurs herein much earlier in thickness than for less adhesive noble metals.[22,33,50] In a more quantitative analysis, SDRS profiles have been fitted (Figure 2-a,b) in the framework of the *GranFilm*[62,65] package using tabulated dielectric constants[78] and extra-broadening of about 1 eV to account for polydispersity[33,64] (see Section SII). The evolutions of film thickness, surface coverage and A_r are reported in Figure 3 as a function of the Cr thickness determined by XPS. The one-to-one correlation (Figure 3-a, slope 0.9) between SDRS and XPS thicknesses validates the approach. The absence of plasmonic response at the onset of Cr deposition, up to $\sim$ 0.5 Å (Figure 3-a), is attributed to oxidation by reaction with surface OH;[47] the formation of defined Cr^{3+}-O_2H moities was evidenced by X-ray absorption combined to *ab initio* calculations,[47] while photoemission revealed that Cr is oxidized but does not reduce alumina.[47,77] Similar reactions are observed at various metal/oxide interfaces[79] and, more specifically, for Rh,[80] Cu,[81,82] Co,[36] Zn,[45] Ti and Al[22,83] on α-Al_2O_3(0001).

As regards to the aspect ratio A_r, the evolution from high values at the onset of the growth to a minimum around 1-2 Å, and a final regular increase (Figure 3-c) parallel the U-shaped curve of $\mathcal{A}_s(t)$ (Figure 2-c). At a Cr thickness of 10 Å, the analysis based on the quasi-static approximation becomes inconsistent (shaded regions in Figure 3), likely because the film percolates as also suggested by the disappearance of charge effects in photoemission. From a truncated sphere model of the Cr cluster, a wetting angle $\theta_e(\mathrm{Cr}|Al_2O_3) = 37°$ is obtained from the minimum value $A_r = 5$ (Figure 3-c). This value is much smaller than that $\theta_e(\mathrm{Cr}|Al_2O_3) = 109°$ derived from the calculated adhesion energy $W(\mathrm{Cr}|Al_2O_3) = 1.85$ J/m^2 (average of References 45,84) by applying the Young-Dupré equation $W(\mathrm{Cr}|Al_2O_3) = \gamma(\mathrm{Cr})(1+\cos\theta_e)$ with a Cr surface energy $\gamma(\mathrm{Cr}) = 2.75$ J/m^2 (average of References 45,84). The difference is however explained by the Markow and Kaischew's idea[31] that the Bauer criterion of 2D growth[28] has to be modified[31] by including the free enthalpy released during condensation $\Delta\mu$ which, applied to Cr, gives:

$$\gamma(Al_2O_3) > \gamma(\mathrm{Cr}) + \gamma(\mathrm{Cr}|Al_2O_3) - \frac{\Delta\mu}{A} \quad (2)$$

or

$$\cos\theta_e > 1 - \frac{\Delta\mu}{A\gamma(\mathrm{Cr})} \quad (3)$$

where A is the contact area of a metal atom at the interface. $\Delta\mu = kT_s\ln(\eta)$ scales with the supersaturation factor $\eta = p(T_{ef})/p(T_s)$ where $p(T_{ef})$ ($p(T_s)$) is the Cr vapor pressure at the effusion (substrate) temperature. Despite strong uncertainties in the extrapolation of the Cr vapor pressure[85] at low temperature ($\eta \approx 50$), the inequality is easily fulfilled. Combined with the low diffusivity (low homologous temperature $T_h(\mathrm{Cr}) = 0.14$[86,87]), this supersaturation effect explains the spreading of growing Cr particles and the two following points which, apparently contradictory, are in fact complementary: (i) Cr does not wet alumina as evidenced by SDRS (Figure 3-c) in agreement with thermodynamics[28,31,32] and numerical simulations;[45,84] (ii) the percolation observed at a Cr thickness of about 10 Å (Figure 3) corresponds to an out-of-

equilibrium behavior similar to that observed for Ti/, Al/[22,35] and Co/alumina[36] as mentioned in the introductory section.

3.2 Zinc sticking coefficient and chemical state

The fraction of the $\sim$ 15 Å evaporated dose of Zn which sticks on Cr/α-Al_2O_3(0001) was quantified by photoemission using a continuous film model (Figure 4) although, at the onset of growth, this only indicates trends for Zn growing in the form of 3D particles. At Cr film thicknesses of less than 0.3 Å, the absence of sticking of Zn (Figure 4) is assigned to the oxidation of Cr at the onset of the growth[47] since Zn hardly condenses on purposely oxidized Cr films (green triangle in Figure 4). The observation is supported by *ab initio* calculations of separation energies at the Zn/M and Zn/MO_x interfaces (M for metal and MO_x for oxide)[44] which showed that oxidation lowers the number of favorable metal/buffer bonds. As a rule of thumb, the reduction of the metallic Cr contribution, due to its oxidation, to Zn adhesion must be systematically accounted for. At higher Cr film thickness, the condensed fraction of Zn increases steeply up to $\sim$ 80 % for a Cr coverage of 0.7 Å and then more slowly. In stark contrast to the bare surface on which Zn does not bind at all at 300 K,[45,48,49] minute fractions of Cr monolayer entail an almost complete sticking of the impinging zinc, which reveals zones of Cr influence which greatly exceed the actual covered surface (Figure 4). As the Cr film percolates above $\sim$ 10 Å (Section 3.1), Zn entirely sticks on the surface. In what follows, Section 3.4 is devoted to the influence of Cr pre-deposition on Zn growth mode.

The known improvement in Zn/alumina adhesion by an activated reaction with surface OH[42,45] suggests analyzing the chemical state of Zn which, because of the marginal chemical shift between Zn^0 and Zn^{2+} (0.1 eV on Zn 2p[88]), is commonly examined in XPS[45] via Auger line shapes and parameter $\alpha_{Zn} = E_B(Zn\,2p_{3/2}) + E_K(ZnL_3M_{45}M_{45})$. Herein, the observed Zn $L_3M_{45}M_{45}$ Auger profile[45,89–94] (not shown) and the value $\alpha_{Zn} = 2013.8 \pm 0.3$ eV (to be compared to tabulated[88] 2013.9 ± 0.25 eV for metallic Zn and 2010.15 ± 0.4 eV for ZnO) unambiguously demonstrate that Zn is metallic at all stages. Therefore, the dramatic improvement of the sticking of Zn on alumina (Figure 4) by a tiny amount of Cr only relies on the presence of metallic Cr.

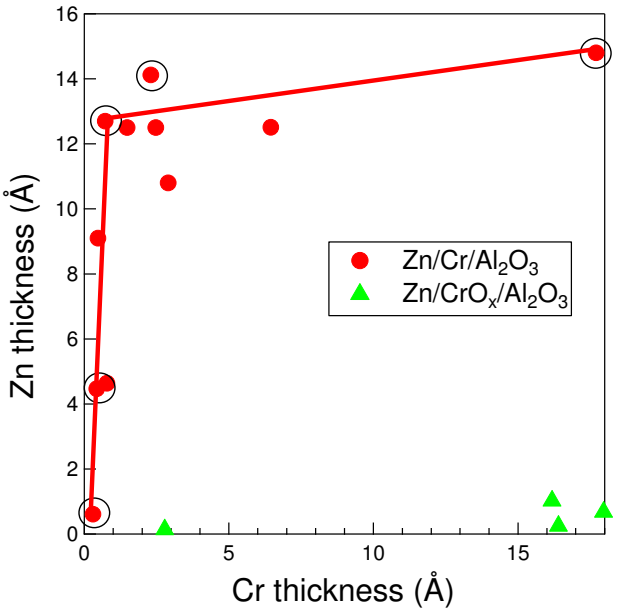

Figure 4: Correlation between the Zn condensed amount after an exposure to a constant nominal thickness of Zn (15 Å) and the Cr predeposited thickness, either metallic (red circles) or oxidized (green triangle). All experiments are performed at 300 K. Oxidized Cr thickness is defined for a Cr_2O_3 composition. Circled points correspond to films studied by SDRS.

3.3 Chromium-induced enhancement of the zinc desorption energy

Zn films deposited on Cr-precovered Al_2O_3(0001) have been desorbed between 300 and 700 K, reconstructed aluminas being models for dry surfaces in parallel to the partially hydroxylated[47] (1×1) alumina (Figure 5-a). Since Zn sticking changes with Cr thickness (Figure 4), the exposure time to Zn vapor was adapted

to reach a condensed amount of Zn of about two monolayers to focus on the impact of the Zn/Cr interface and to limit "bulk" Zn signal. On the two thick Cr films purposely oxidized prior to an exposure to a Zn nominal thickness of $\sim$ 45 Å, the tiny amount of desorbed Zn confirms the low Zn sticking on this surface at 300 K ($\sim$ 0.5 Å; Figure 4). The oxidized Cr films (green lines in Figure 5) give rise to two desorption peaks but, owing to the small amount of adsorbed Zn, the analysis was restricted to the most intense feature. On the (1×1) surface, the Zn desorption peak shifts from 470 to 570 K, broadens and gets asymmetric upon increasing Cr thickness (Figure 5-a). On thick Cr films, the multicomponent desorption lines (red curves in Figure 5) suggest an alloying effect involving Zn-rich Zn_xCr_y compounds found in the bulk phase diagram below 700 K. In the same way, high desorption temperatures of Zn on Ag, Cu, Ni, Rh, Rh, Pt, Pd[95–99] were attributed to alloying with supports. Finally, the overlap at a given Cr thickness of desorption signals normalized in intensity and position for both (1 × 1) and reconstructed surfaces demonstrates a similar Zn bonding dominated by metallic Cr (Figure 5-b).

Any O_2 desorption is excluded since double ionization (Zn^{2+}; $m/e = 32$) leads to the same line shape as Zn^+. No noticeable ZnO ($m/e = 80$) signal was observed. Zn is completely eliminated upon desorption, as demonstrated by the XPS analysis of Zn 2p whose high photoionization cross section guarantees a high sensitivity (Table S1). This contrasts with the desorption of Zn adsorbed at 100 K on the partially hydroxylated (1 × 1) alumina, where a fraction of Zn oxidizes by reaction with surface OHs and binds very strongly to the surface (desorption at $\simeq$ 1300 K).[45] In the present case, Zn adsorbed on Cr-precovered alumina remains fully metallic and completely desorbs below 600 K. The lack of Cr desorption signal ($m/e = 52$) and the constant Cr amount and XPS Cr 2p line shape before and after desorption (not shown) rules out any substantial reaction with the substrate[100] and confirms the thermal stability of Cr expected from its low vapor pressure ($p_{Cr} \ll 10^{-11}$ mbar at 700 K as compared to $p_{Zn} \simeq 10^{-1}$ mbar).

Desorption activation energies E_a determined by leading-edge analysis are compared to results obtained after Zn condensation on bare (1 × 1) and reconstructed surfaces at 100 K[45,49] (Figure 6). An example of TPD analysis [a] is given in Figure S6. In a broken bond model, estimates of E_a are $9/12E_{coh}$(Zn) for a Zn atom on a (0001) plane, $7/12E_{coh}$(Zn) on the $[10\bar{1}0]$ step on a (0001) surface and $4/12E_{coh}$(Zn) for a kink atom since the coordination number of 12 for the hexagonal compact Zn reduces to 9, 7 and 4 for surface, step and kink, respectively. On dry reconstructed bare surfaces, the experimental values of E_a that lie between $7/12 - 9/12E_{coh}$(Zn) convey a poor interaction with the substrate that is partly improved upon hydroxylation[45] (open versus filled red circles, Figure 6). Significantly, in the presence of Cr, E_a values are of the order of E_{coh}(Zn) and well above those found on Cr free surfaces (blue symbols, Figure 6), which is assigned to strong Zn-Cr bonds combined to neighboring Zn-Zn interactions.[44] Finally, while the Zn hardly sticks on oxidized Cr, the sizeable values of E_a (green symbols in Figure 6) reveal a strong interaction of Zn with defects at that surface.

3.4 Plasmonics for real time analysis of Zn spreading on $Cr/Al_2O_3(0001)$

The study of the Zn adsorption on Cr-precovered $Al_2O_3(0001)$ focuses on Cr film thicknesses of 0.3, 0.43, 0.7, 2.3 and 17.7 Å (circled points in Figure 4) judged representative of the Cr effect. In final spectra (Figure 7),

[a] The Redhead method (see Figure S7) based only on desorption peak position overestimates E_a which, in a picture of quasi-equilibrium between adsorption and desorption, should not be greater than the bulk cohesive energy of zinc E_{coh}(Zn) = 1.35 eV.atom^{-1} (Reference 101). Moreover, the desorption order is systematically found close to zero instead of $n = 1$ assumed by Redhead analysis,[75] if one excepts the thickest Cr layers for which $n \simeq 2$.

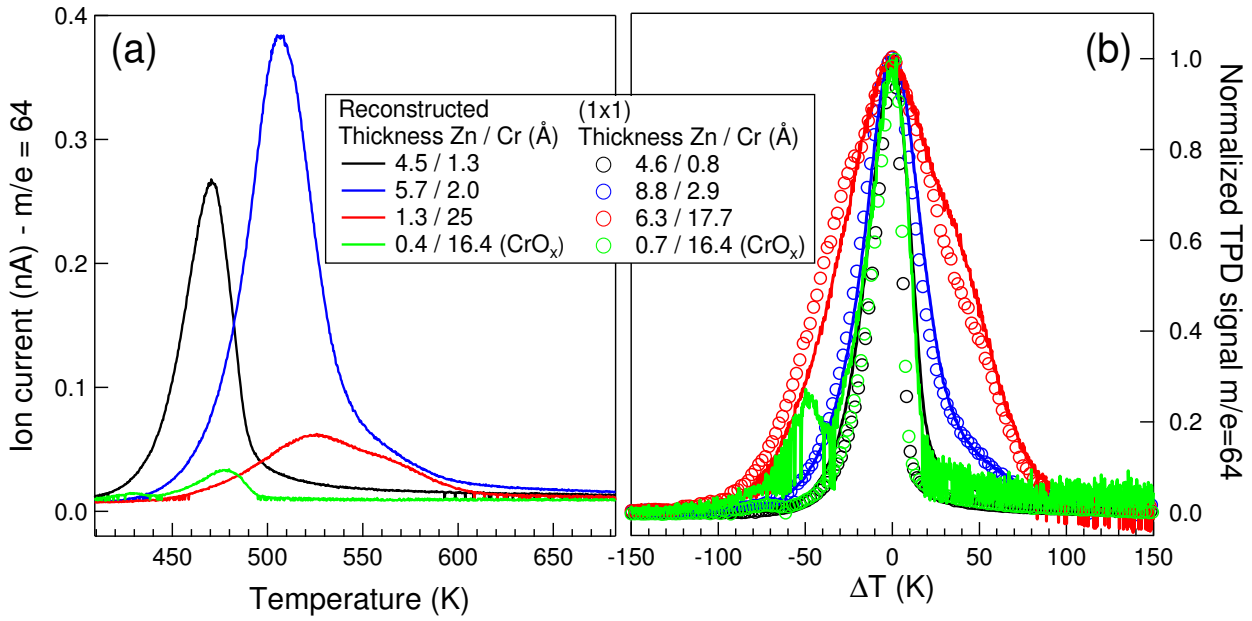

Figure 5: Desorption spectra of Zn ($m/e = 64$): (a) desorption spectra from reconstructed alumina (solid lines); (b) desorption peaks normalized to peak maximum and position for Cr-covered (1×1) (markers) and reconstructed alumina surfaces (solid lines). Film thicknesses are given in the figure. The heating rate is $\alpha = 0.33$ K.s^{-1}.

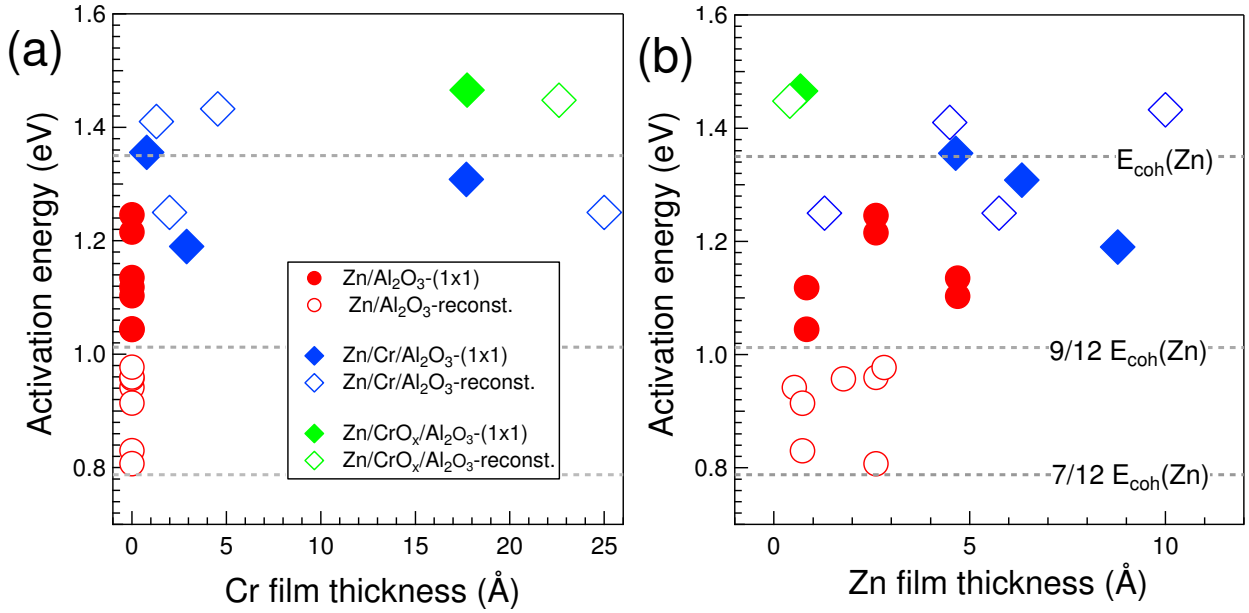

Figure 6: Zn desorption activation energies deduced from the leading edge analysis as a function of (a) Cr and (b) Zn film thickness for (1×1) (filled symbols) and reconstructed surfaces (open symbols). Data are compared to the bare surface case[45,49] (red points) and the cohesive energy of Zn (dotted lines; see text). Despite the thermal contact between the insulating alumina and the heated back plate (estimated to $\Delta T \sim 50$ K), the uncertainties on the determined energies remain always well below fluctuations due the reproducibility of initial thicknesses and morphologies.

the increase in intensity of the resonance corresponds to an increase in Zn condensed amount with Cr thickness. Notice that, beyond the amplitude, final SDRS line shapes are also impacted by the initial coverage in Cr (Figure 7-a). All spectra exhibit an asymmetric broad band typical for the plasmonic response of Zn nanoparticles[45,57] that mainly consists in a parallel dipolar absorption mode excited on the Zn interband transitions.[57]

In Figure 7, the progressive shift of the SDRS resonance from 3.9 to 1.6 eV as the Cr film thickens (and hence the Zn film) indicates a high sensitivity to A_r and spreading of Zn particles. To overcome the discontinuity of the Cr layer which makes the dielectric simulation of the $Zn/Cr/Al_2O_3$ stack intractable, trends were derived from simulations of Zn/alumina (Figure 7-b). As supported by dipolar modeling,[77] this simplification is all the more relevant as Cr deposits are thinner. Zn particles were modeled by truncated spheres and spheroids of increasing aspect ratios without accounting for particle-particle interaction and size/shape broadening (Section SII). The average thickness of Zn film (15 Å) was kept constant in simulations. As compared to expectation for a continuous film (Figure 7-b, red line), the energies of the broad bands observed in the ultra-violet/visible range point to a 3D growth mode; their progressive redshift demonstrates that Zn particles flatten upon increasing Cr thickness. Values of aspect ratio $A_r < 2$, 2 and > 8 are assigned to Zn(0.6 Å)/Cr(0.3 Å) (Figure 7; grey line), Zn(4.5 Å)/Cr(0.43 Å) (Figure 7; green line), Zn(14.1 Å)/Cr(2.3 Å) (Figure 7; light blue line) stacks, respectively. To highlight the promotion of Zn wetting by Cr, comparisons are made with the Zn deposition on bare alumina at 100 K (Figure 7, black circles) and on the purposely oxidized Cr film (Figure 7-a, black squares). At 100 K, Zn readily sticks[45] but forms cluster of $A_r \sim 4$ indicative not only of a non-wetting behavior but also of a sizable spreading due of reduced mobility and out-of-equilibrium growth conditions, with an homologous temperature close to that of Cr at 300 K [$T_h(\mathrm{Zn}; 100\mathrm{K}) = 0.14$; $T_h(\mathrm{Zn}; 300\mathrm{K}) = 0.43$; $T_h(\mathrm{Cr}; 300\mathrm{K}) = 0.14$]. A similar A_r is observed for Zn deposited on the oxidized Cr film. Together with the low sticking of Zn (Figure 4), this demonstrates that Cr oxidation is detrimental to Zn wetting.

Now, to analyze the formation of Zn films, advantage was taken of the ability of SDRS for real-time analysis. Evolutions of SDRS spectra recorded all along Zn growth on $Cr/Al_2O_3(0001)$ surfaces are compared in Figure 8. The integrated SDRS signal $\mathcal{A}_s$ defined by Equation 1 (Figure 9) provides, as in the case of the Cr growth (Section 3.1), a continuous representation of the evolution of A_r. The U-shape of $\mathcal{A}_s$ features a 3D growth regime[50] (except for the Zn/Cr(17.7 Å) film). The first branch of the "U" is assigned to a size-dependent equilibrium shape related to surface/interface stress effects[50] at a about constant density of islands dictated by the pre-deposited Cr. The second branch of the "U" stems from coalescence.[50] Among the cases selected, two very different behaviors can be distinguished, a steep increase in Zn sticking observed for minute amounts of pre-deposited Cr (0.3, 0.43 and 0.7 Å) and then a slower change for Cr thickness of 2.3 Å or higher (Figure 4), that are separately discussed in what follows.

3.4.1 The seed layer

On the 0.3 Å Cr pre-deposited layer, which covers only a few percent of the surface (Figure 3-b), Figure 7-a shows that there is about as much deposited Zn as on the oxidized Cr film, which means that Cr clusters capture zinc much more efficiently than the oxide in proportion to their relative surface. Since these Cr clusters are mostly oxidized,[47,77] the sticking of Zn likely relates to the small proportion of metallic Cr they contain. The value of $A_r \sim 1.25$ derived from the position of the resonance (Figure 7) corresponds to a wetting angle $\theta_e(\mathrm{Zn}|\mathrm{Al_2O_3}) \sim 127°$ which is in fair agreement with the prediction of 125° (adhesion energy of 0.23 J/m^2 and Zn surface energy of 0.54 J/m^2) for Zn/hydroxylated

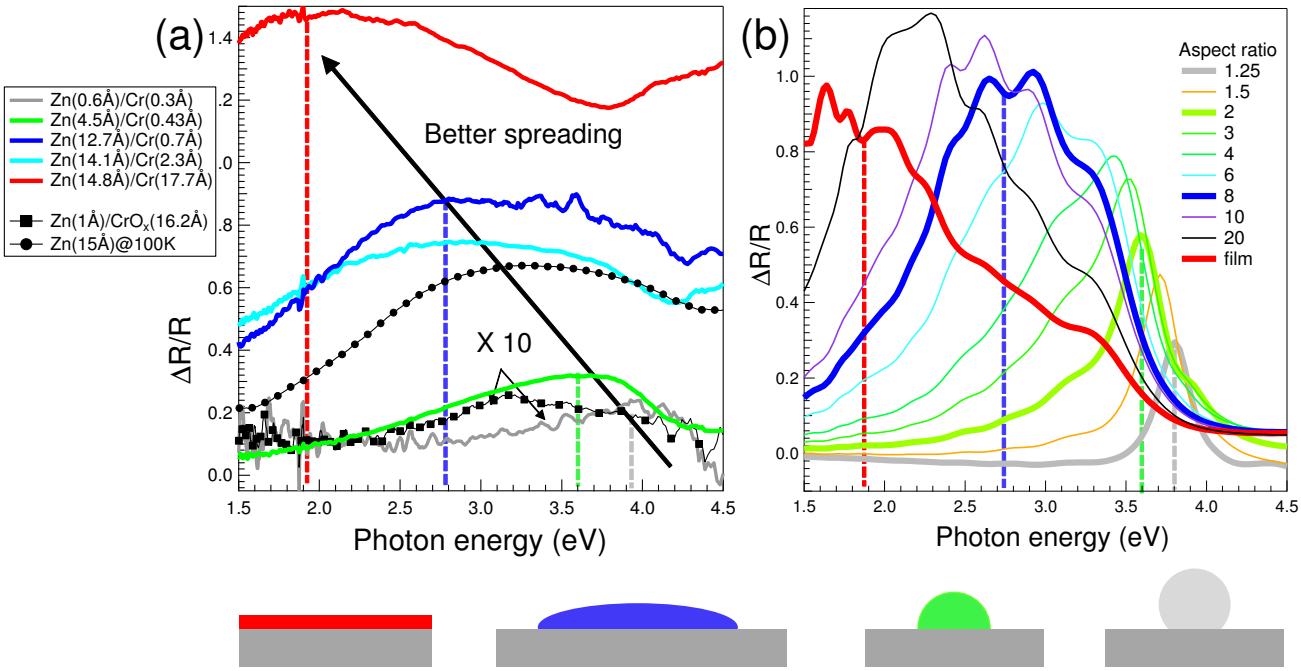

Figure 7: (a) Differential reflectivity spectra of $Zn/Cr/Al_2O_3(0001)$ in s-polarization recorded after the exposure of Cr-precovered substrates to a constant nominal thickness of Zn ($\sim$ 15 Å). Actual condensed thicknesses as calibrated by photoemission are given in the figure. All spectra are referenced to the bare alumina spectrum. The comparison is made to spectra recorded during Zn growth on Al_2O_3 at 100 K (incident angle of $\theta_0 = 55°$; Reference 45) and on an oxidized Cr film (black curves); (b) Simulated s-polarized spectra for Zn/Al_2O_3 nanoparticles of different aspect ratios A_r. Truncated sphere shape is used for $A_r < 2$ and oblate hemispheroid for $A_r > 2$ (see schematics). In simulations of Figure b, the average film thickness is kept constant at 15 Å and a comparison is made with the response of a continuous thin film of same thickness (red line). The position of the resonance (dotted vertical lines) allows to estimate particle aspect ratios.

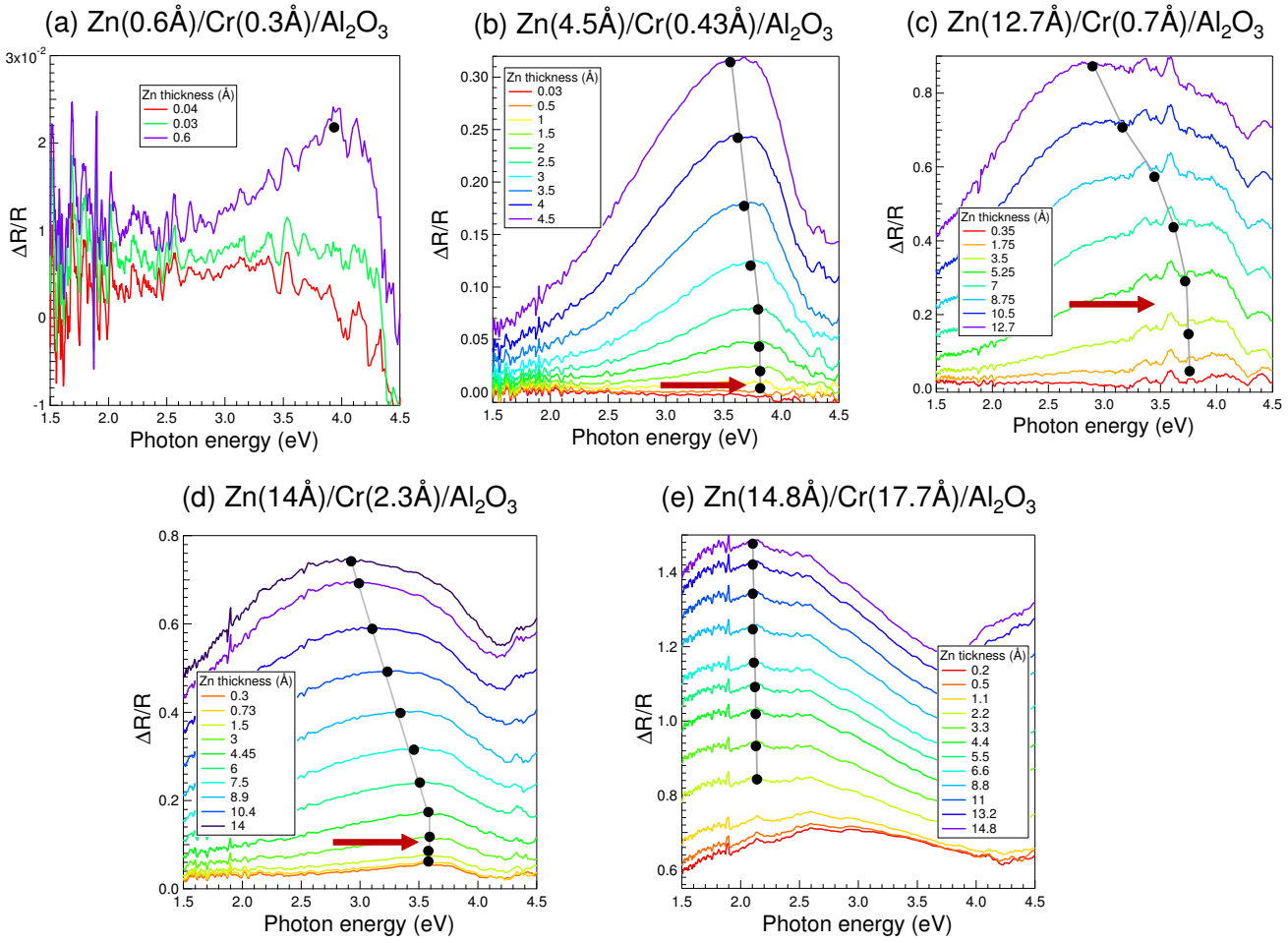

Figure 8: Evolution of the SDRS spectra (s-polarization) during the growth of Zn on Cr-precovered substrates. Spectra are normalized to the bare substrate reflectivity so that the first spectrum corresponds to that of the Cr deposit. The Zn film thicknesses indicated in the figure on each spectrum have been deduced by photoemission by assuming a constant sticking probability, *i.e.* deposited amounts that scale with time. Red arrows show the position of the minimum of the integrated SDRS signal $\mathcal{A}_s$ (Figure 9).

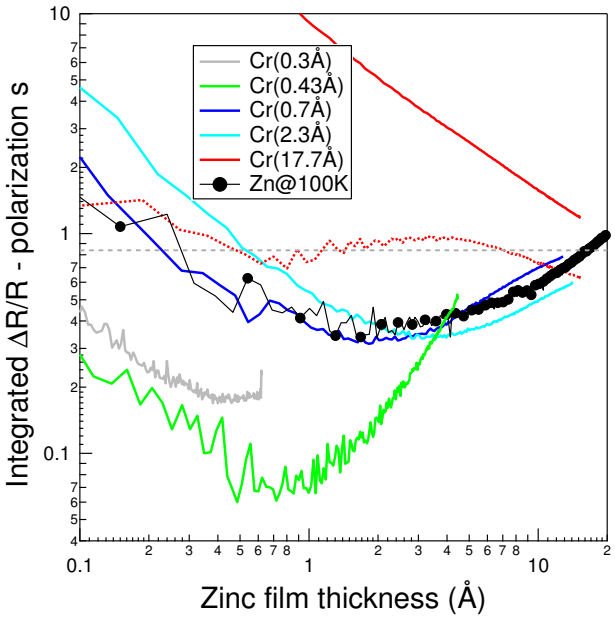

Figure 9: Evolution of the integrated SDRS signal $\mathcal{A}_s$ as a function of average Zn thickness on various Cr-precovered substrates. The red-dotted line corresponds to the Cr subtracted signal $\mathcal{A}_s^{Zn}$ of the Zn(14.8 Å)/Cr(17.7 Å) deposit (see text for definition; Equation 4). It is compared to the theoretical expectation from the tabulated dielectric function of zinc (Equation 5; horizontal grey dotted line).

$Al_2O_3(0001)$;[46] on the contrary, it differs unambiguously from $\theta_e(Zn|Al_2O_3) = 78°$ expected for Zn/dry Al-terminated alumina (adhesion energy 0.65 J/m^2).[46] Therefore, Zn clusters can be seen as anchored to metallic Cr but in contact with the hydroxylated alumina surface which dictates the observed contact angle (aspect ratio) under the reasonable assumption that not all the surface OH have been reacted by the small deposited amount of Cr. Consistently, in Figure 9, the lack of second branch in the "U" points to the absence of coalescence[50] on a surface which only presents a minute coverage of metallic Cr.

On the 0.43 Å thick Cr/alumina film (Figure 8-b), the final Zn thickness amounts to 4.5 Å accordingly to Figure 4. The mild variation of the Zn resonance energy (Figure 8-b) from 3.8 to 3.65 eV is associated to A_r ($\theta_e(Zn|Al_2O_3)$) ranging from 1.25 to 2 (127 to 100°). As on the 0.3 Å thick Cr film, Zn clusters can be viewed as anchored on widely dispersed small Cr islands although with a higher Cr metal/oxide ratio. At the onset of their growth, the contact angle $\theta_e(Zn|Al_2O_3) = 127°$ shows that they are mainly in contact with a hydroxylated surface. Upon increasing Zn thickness, the increase in A_r from 1.25 to 2 indicates a partial coalescence. The final Zn amount of $\sim$ 30% of the dose is far too strong to stem from a direct sticking of Zn on the Cr islands that cover less than $\sim$ 5% of the surface while Zn does not adsorb on the bare alumina.[45,48] This suggests a residence time of physisorbed Zn long enough to allow a high probability of binding to existing Cr (Cr-Zn) clusters or, in other words, a diffusion length of Zn adatoms of the order of the mean distance between the metallic spots of Cr. Figure 9 indicates that the aspect ratio of Zn/Cr(0.43 Å) particles remains rather low (low integrated $\mathcal{A}_s$ value) despite a flattening at the end of the growth process (second branch of the "U") which corresponds to a coalescence beyond the position of the minimum of the "U" as indicated by the red arrow (see also Figure 8-b).

Similar but more accentuated phenomena are observed on the 0.7 Å thick Cr film (Fig-

ure 8-c). The shift from 3.65 to 2.75 eV of the resonance corresponds to A_r ($\theta_e(\mathrm{Zn}|\mathrm{Al_2O_3})$) ranging from 1.75 to 8 (100 to 30°). With a initial wetting angle halfway between those related to hydroxylated (125°; Reference 45) and bare (78°; Reference 46) alumina, Zn clusters likely start to grow on a partially hydroxylated surface since higher the Cr coverage, lower the OH coverage. The higher density of metallic Cr seeds likely tends to flatten Zn particles. Consistently, the increase as a whole of the integrated intensity $\mathcal{A}_s$ (Figure 9) is indicative of such a flattening of Zn clusters with respect to observations made at lower Cr thickness. Then, the shift to higher Zn thickness of the minimum of $\mathcal{A}_s$ (Figure 9) means that a larger quantity of Zn is present at the onset of the coalescence (the second branch of the "U"). The final increase in A_r of Zn clusters to higher values than observed at lower Cr thickness (Figure 9) evidences a more pronounced incomplete coalescence *i.e.* flatter objects.[102,103] Therefore, at 300 K, a partly oxidized 0.7 Å thick Cr film, that covers only $\sim 5\%$ of the alumina surface (Figure 3-b), allows the capture of more than 80 % of a Zn dose. This rules out a sticking mechanism driven only by direct impact but rather supports the previous assumption of a long residence time on the alumina surface of the impinging Zn atoms with, in the present case, a diffusion length larger than the average distance between Cr islands.

Figure 10 sums up schematically the impact of the Cr clusters on Zn sticking and wetting in the above three cases. The metallic layer can be termed seed layer in that the few percents of metallic Cr promotes an almost complete Zn sticking on an alumina surface which does not otherwise bind this metal. The way Zn grows on pre-deposited Cr suggests an encapsulation of Cr by Zn while TPD points at a desorption energy above the cohesion energy of Zn. Larger Cr surface energy compared to Zn (see above), sizable adhesion energy[46] ($W(\mathrm{Cr}|\mathrm{Zn}) = 3.11$ J/m^2) and stronger Zn-Cr than Zn-Zn bonds (interface energy[46] $\gamma(\mathrm{Cr}|\mathrm{Zn}) = -0.51$ J/m^2) explain both findings. In line with the hierarchy of enthalpy of formation of their oxides ($\Delta H(\mathrm{Cr_2O_3}) = -1134.7$ kJ/mol; $\Delta H(\mathrm{ZnO}) = -350.46$ kJ/mol) and first-principle atomistic calculations,[42,44,45] Cr forms stronger bonds than Zn with the alumina surface. Therefore, the enhancement of the spreading of Zn/alumina at 300 K does not stem from the wetting by Cr, as poor as that of Zn on bare alumina at 100 K, but from the strength of the bonding at the successive interfaces. Such seed layers are of interest in several respects: (i) they can be anticipated to mildly affect the intrinsic properties of the film whose sticking and spreading are favored; (ii) they offer a very flexible method of preparing a 3D particle distribution; (iii) most importantly, they are likely representative of realistic cases in which, due to environment, a pure continuous layer of an additive prone to oxidation can hardly be prepared.

3.4.2 The adhesion layer

Above 1.5 Å (see Figure 3) Cr grows as high aspect ratio islands ($A_r(\mathrm{Cr}) \simeq 5$) which cover progressively the surface before percolating around 10 Å. Consistently, Zn particles start flattening at the onset of deposition on 2.3 Å of Cr and flatten even further as the buffer percolates (Figure 8-d). Incidentally, the "U" curve associated to Zn deposition at 100 K where kinetics plays a role shows a rather similar shape as those corresponding to 0.7 and 2.3 Å of Cr (Figure 9).

On the percolated 14.8 Å thick Cr film (Figure 8-e), estimates of $A_r(\mathrm{Zn}) \simeq 5; 8; 10$ for Zn thicknesses of 0.2, 0.5 and 1.1 Å obtained by comparison to simulations (Figure 7-b) indicates a good spreading. At Zn thicknesses larger than 2.2 Å, the nearly homothetic SDRS profile matches with a continuous morphology (red line in Figure 7-b versus Figure 8-e). In fact, the spectrum of the Zn(14.8 Å)/Cr(17.7 Å) film is nicely accounted for by a continuous film morphology as shown by the agreement with the dielectric simulations of a stack of 2D films whose thicknesses are

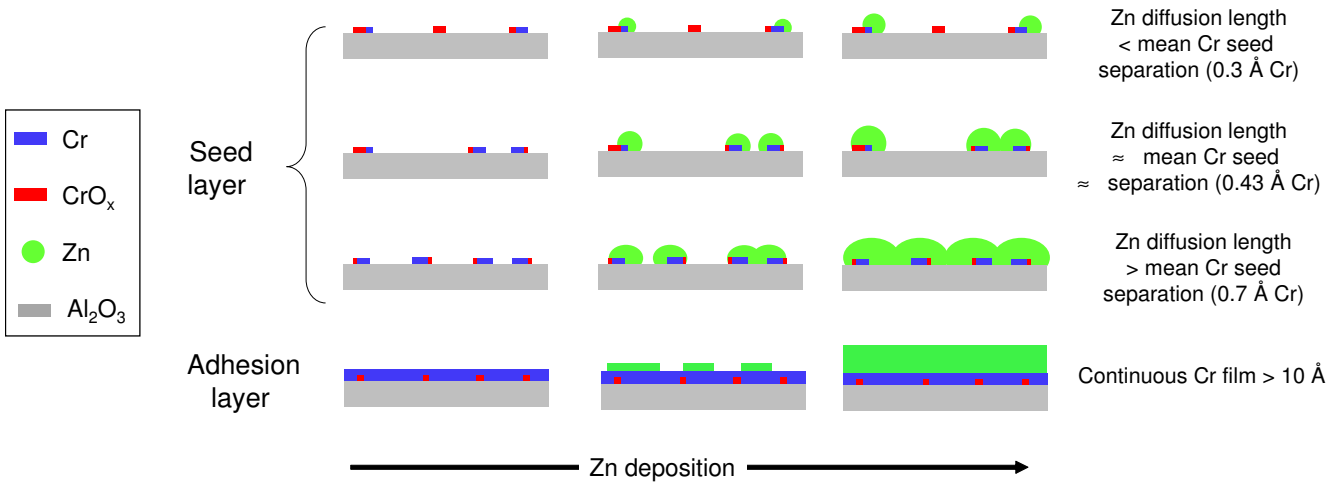

Figure 10: Schematic evolution of the Zn layer morphology as a function of Cr thickness (left: no Zn; middle: intermediate Zn thickness; right: full Zn dose).

those given by the XPS measurements (see Figure S5). Finally, a continuous decrease of the corresponding integrated $\mathcal{A}_s$ is observed (Figure 9). In contrast to other samples, the spectra contain a strong initial Cr contribution (see first spectrum in Figure 8-e). Owing to the additivity of the first order surface susceptibilities for a stack of films,[58,104] the Cr contribution can be subtracted as follows:

$$\mathcal{A}_s^{Zn}(t_{Zn}) = \mathcal{A}_s(t_{Zn}) - \frac{t_{Cr}}{t_{Zn}}\mathcal{A}_s^{Cr}(t_{Cr}), \qquad (4)$$

where $\mathcal{A}_s^{Zn}$ is the contribution of the Zn film alone, $\mathcal{A}_s^{Cr}$ that of the Cr film before Zn growth and t_{Zn}, t_{Cr} the average thicknesses of the two films. The subtracted signal $\mathcal{A}_s^{Zn}(t_{Zn})$ (Figure 9; red dotted line) does not follow the previous highlighted behavior for nanoparticles[50] but is nearly constant as expected for the case of a thin continuous film. Indeed, for such a morphology, the integrated signal scales only with the imaginary part of the material dielectric constant[50,57] (Figure S4-a):

$$\mathcal{A}_s(t_f) = \int_0^\infty \mathrm{Im}[\epsilon_{Zn}(\omega)]d\omega. \qquad (5)$$

The experimental value is close to the integral of the tabulated Zn dielectric function,[105] which appears as the limit value for all deposits. The nearly layer-by-layer growth mode suggested by the integrated signal is confirmed by the series of homothetic SDRS spectra observed above a Zn thickness of 2.2 Å (Figure 8-e). Therefore, above 10 Å, percolated Cr films that nearly fully cover the alumina surface form what can be called perfect adhesion layers for Zn (see Figure 10).

4 Conclusion

A detailed analysis of the chemical state, sticking and spreading/wetting of Zn on Cr predeposited film on α-Al_2O_3(0001) at 300 K has been performed by a combination of surface sensitive techniques involving surface differential reflectivity spectroscopy. Beyond its ability to analyze the morphology of very small supported clusters, the technique has demonstrated its flexibility in monitoring the growth of multimetallic films. At the onset of the Cr deposition, the oxidation of Cr by reaction with the surface OH is very detrimental for Zn sticking. Being nil on the bare alumina surface, the sticking coefficient of metallic Zn shows two very distinct behaviors, which do not scale at all with the metallic Cr coverage:

- at very low coverages, metallic chromium acts as a seed layer which captures Zn atoms that diffuse over the surface, leading to a steep increase of the Zn sticking and a Zn spreading that far exceeds the

Cr coverage. Zn clusters are anchored on the Cr seeds that they encapsulate, but their wetting behavior is dictated by the contact with alumina. As an example, the pre-deposition of 0.7 Å of Cr covering $\sim$ 5% of the alumina surface allows the capture of $\sim$ 80% of a Zn dose of 15 Å.

- at increasing film thicknesses, Cr forms high aspect ratio islands that cover progressively the surface before percolating around 10 Å. At this point, the Cr film behaves as an adhesion layer. In the limit of the optical measurements, Zn growth mode is found to be 2D; Zn perfectly wets the Cr-covered alumina surface.

The ability of tiny amounts of metal to dramatically enhance the sticking of a film is of great practical interest. Firstly, it shows that under realistic conditions in which the growth of a full metallic buffer adlayer cannot be achieved, a non-continuous and partially oxidized layer can induce sufficient sticking. In a very different perspective, the anchoring of a layer by discrete seeds can keep the properties of the film intact, which is often desired. Finally, such anchoring offers a method for preparing a 3D particle distribution. The mechanisms highlighted herein are quite general since, as metals used in buffers do no wet large band gap oxides, their efficiency relies on the strength of the buffer-substrate and film-buffer bonds.

Acknowledgement We are grateful to Jacek Goniakowski (INSP) for fruitful discussions on the energetics of metallic particles. This work was supported by French state funds managed by the ANR within the Investissements d'Avenir programme under reference ANR-11-IDEX-0004-02, and more specifically within the framework of the Cluster of Excellence MATISSE led by Sorbonne Universités.

Supporting Information Available

The Supporting Information is available free of charge at XXX
SI : Photoemission quantification; SII: Surface Differential Reflectivity Spectroscopy; SIII: Temperature Programmed Desorption.

References

(1) Barmak, K., Coffey, K., Eds. *Metallic films for electronic, optical and magnetic applications*; WP Woodhead Publishing, 2014.

(2) Campbell, C. T.; Parker, S. C.; Starr, D. E. The effect of size-dependent nanoparticle energetics on catalyst sintering. *Science* **2002**, *298*, 811.

(3) Fu, Q.; Wagner, T. Interaction of nanostructured metal overlayers with oxide surfaces. *Surf. Sci. Rep.* **2007**, *62*, 431–498.

(4) Evans, A. G.; Hutchinson, J. W.; Wei, Y. Interface adhesion: effects of plasticity and segregation. *Acta Mater.* **1999**, *47*, 4093–4113.

(5) Abadias, G.; Chason, E.; Keckes, J.; Sebastiani, M.; Thompson, G. B.; Barthel, E.; Doll, G. L.; Murray, C. E.; Stoessel, C. H.; Martinu, L. Review Article: Stress in thin films and coatings: Current status, challenges, and prospects. *J. Vac. Sci. Technol., A* **2018**, *36*, 020801.

(6) Thompson, C. V. Solid-state dewetting of thin films. *Annu. Rev. Mater. Res.* **2012**, *42*, 399–434.

(7) Jacquet, P.; Podor, R.; Ravaux, J.; Teisseire, J.; Gozhyk, I.; Jupille, J.; Lazzari, R. Grain growth: the key to understand solid-state dewetting of silver thin films. *Scr. Mater.* **2016**, *115*, 128 – 132.

(8) Jacquet, P.; Podor, R.; Ravaux, J.; Lautru, J.; Teisseire, J.; Gozhyk, I.; Jupille, J.; Lazzari, R. On the solid-state dewetting of polycrystalline thin films: capillary versus grain growth approach. *Acta Mater.* **2018**, *143*, 281 – 290.

(9) Henriquez, R.; Roco, R.; Bravo, S.; Del Campo, V.; Gonzalez-Fuentes, C.; Donoso, S.; Häberle, P. Effect of a metallic surfactant on the electrical percolation of gold films. *Appl. Surf. Sci.* **2019**, *489*, 403–408.

(10) Kästle, G.; Boyen, H. G.; Koslowski, B.; Plettl, A.; Weigl, F.; Ziemann, P. Growth of thin, flat, epitaxial (111) oriented gold films on c-cut sapphire. *Surf. Sci.* **2002**, *498*, 168–74.

(11) Chen, W.; Chen, K. P.; Thoreson, M. D.; Kildishev, A. V.; Shalaev, V. M. Ultrathin, ultrasmooth, and low-loss silver films via wetting and annealing. *Appl. Phys. Lett.* **2010**, *97*, 211107.

(12) J., L. V.; Kobayashi, N. P.; Islam, M. S.; Wu, W.; Chaturvedi, P.; Fang, N. X.; Wang, S. Y.; Williams, R. S. Ultrasmooth silver thin films deposited with a germanium nucleation layer. *Nano Letters* **2009**, *9*, 178–182.

(13) Formica, N.; Ghosh, D. S.; Carrilero, A.; Chen, T. L.; Simpson, R. E.; Pruneri, V. Ultrastable and atomically smooth ultrathin silver films grown on a copper seed layer. *ACS Applied Materials & Interfaces* **2013**, *5*, 3048–3053.

(14) Zhang, J.; Fryauf, D. M.; Garrett, M.; Logeeswaran, V.; Sawabe, A.; Islam, M. S.; Kobayashi, N. P. Phenomenological model of the growth of ultrasmooth silver thin films deposited with a germanium nucleation layer. *Langmuir* **2015**, *31*, 7852–7859.

(15) Zhao, G.; Wang, W.; Bae, T.-S.; Lee, S.-G.; Mun, C.; Lee, S.; Yu, H.; Lee, G.-H.; Song, M.; Yun, J. Stable ultrathin partially oxidized copper film electrode for highly efficient flexible solar cells. *Nat. Commun.* **2015**, *6*, 8830.

(16) Fukuda, K.; Lim, S. H. M.; Anders, A. Coalescence of magnetron-sputtered silver islands affected by transition metal seeding (Ni, Cr, Nb, Zr, Mo, W, Ta) and other parameters. *Thin Solid Films* **2008**, *516*, 4546–4552.

(17) Aouani, H.; Wenger, J.; Gérard, D.; Rigneault, H.; Devaux, E.; Ebbesen, T. W.; Mahdavi, F.; Xu, T.; Blair, S. Crucial role of the adhesion layer on the plasmonic fluorescence enhancement. *ACS Nano* **2009**, *3*, 2043–2048.

(18) Siegfried, T.; Ekinci, Y.; Martin, O. J. F.; Sigg, H. Engineering metal adhesion layers that do not deteriorate plasmon resonances. *ACS Nano* **2013**, *7*, 2751–2757.

(19) Todeschini, M.; Bastos da Silva Fanta, A.; Jensen, F.; Wagner, J. B.; Han, A. Influence of Ti and Cr adhesion layers on ultrathin Au films. *ACS Appl Mater Interfaces* **2017**, *9*, 37374–37385.

(20) Romanyuk, A.; Steiner, R.; Mathys, D.; Thommen, V.; Oelhafen, P. Use of tin as a surfactant material for the growth of thin silver films on silicon oxide. *Surf. Sci.* **2008**, *602*, L49 – L52.

(21) Søndergård, E.; Kerjan, O.; Abriou, D.; Jupille, J. Growth and buffer effects of titanium on silver/α-Al_2O_3(0001). *Eur. Phys. J. D* **2003**, *24*, 343–345.

(22) Lazzari, R.; Jupille, J. Interfacial chemistry and wetting of metallic films on the hydroxylated α-Al_2O_3(0001) surface. *Phys. Rev. B* **2005**, *71*, 045409.

(23) Liu, H.; Wang, B.; Leong, E. S. P.; Yang, P.; Zong, Y.; Si, G.; Teng, J.; Maier, S. A. Enhanced surface plasmon resonance on a smooth silver film with a

seed growth layer. *ACS Nano* **2010**, *4*, 3139–3146.

(24) Dehm, G.; Scheu, C.; Rühle, M.; Raj, R. Growth and structure of internal Cu/Al_2O_3 and $Cu/Ti/Al_2O_3$ interfaces. *Acta. Mater.* **1998**, *46*, 759–771.

(25) Chatain, D.; Coudurier, L.; Eustathopoulos, N. Wetting and interfacial bonding in ionocovalent oxide-liquid metal systems. *Revue Phys. Appl.* **1988**, *23*, 1055–1064.

(26) Yoshitake, M.; Yagyu, S.; Chikyow, T. Novel method for the prediction of an interface bonding species at alumina/metal interfaces. *J. Vac. Sci. Technol., A* **2014**, *32*, 021102.

(27) Hemmingson, S. L.; Campbell, C. T. Trends in adhesion energies of metal nanoparticles on oxide surfaces: Understanding support effects in catalysis and nanotechnology. *ACS Nano* **2017**, *11*, 1196–1203.

(28) Bauer, E. Phaenomenologische Theorie der Kristallabscheidung an Oberflaechen I. *Z. Kristallogr* **1958**, *110*, 372–394.

(29) Chatain, D.; Rivollet, I.; Eustathopoulos, N. Adhésion thermodynamique dans les systèmes non-réactifs métal liquide-alumine. *J. Chim. Phys.* **1986**, *83*, 561–567.

(30) Campbell, C. T. Ultrathin metal films and particles on oxide surfaces: structural, electronic and chemisorptive properties. *Surf. Sci. Rep.* **1997**, *27*, 1–111.

(31) Markov, I.; Kaischew, R. Influence of supersaturation on the mode of crystallization on crystalline substrates. *Thin Solid Films* **1976**, *32*, 163–167.

(32) Lüth, H. *Surface and Interfaces of Solids*; Springer Study Edition; Springer-Verlag Berlin Heidelberg, 1992.

(33) Lazzari, R.; Jupille, J. Growth kinetics and size-dependent wetting of Ag/α-$Al_2O_3(0001)$ nanoparticles studied via the plasmonic response. *Nanotechnology* **2012**, *23*, 135707.

(34) Lazzari, R.; Goniakowski, J.; Cabailh, G.; Cavallotti, R.; Trcera, N.; Jupille, J.; Lagarde, P. Surface and epitaxial stress for supported metal clusters. *Nano Lett.* **2016**, *16*, 2574–2579.

(35) Lazzari, R.; Simonsen, I.; Bedeaux, D.; Vlieger, J.; Jupille, J. Polarizability of truncated spheroidal island supported by a substrate : models and applications. *Eur. Phys. J. B* **2001**, *24*, 267–284.

(36) Chambers, S.; Droubay, T.; Jennison, D.; Mattsson, T. Laminar growth of ultrathin metal films on metal oxides: Co on hydroxylated α-$Al_2O_3(0001)$. *Science* **2002**, *297*, 827–831.

(37) Dai, Z.; Borghetti, P.; Chenot, S.; David, P.; Jupille, J.; Cabailh, G.; Goniakowski, J.; Lazzari, R. Aluminium segregation profiles in the (110), (100) and (111) surface regions of the $Fe_{0.85}Al_{0.15}$ random body-centered cubic alloy. *Appl. Surf. Sci.* **2019**, *492*, 886–895.

(38) Dai, Z.; Alyabyeva, N.; Borghetti, P.; Chenot, S.; David, P.; Koltsov, A.; Renaud, G.; Jupille, J.; Cabailh, G.; Lazzari, R. Al-rich $Fe_{0.85}Al_{0.15}(100)$, (110) and (111) surface structures. *Appl. Surf. Sci.* **2020**, *509*, 145312.

(39) Dai, Z.; Alyabyeva, N.; Van den Bossche, M.; Borghetti, P.; Chenot, S.; David, P.; Koltsov, A.; Renaud, G.; Jupille, J.; Cabailh, G. et al. Oxide at the Al-rich $Fe_{0.85}Al_{0.15}(110)$ surface. *Phys. Rev. Materials* **2020**, *4*, 074409.

(40) Guttmann, M. Diffusive phase transformations in hot dip galvanizing. Reactive phase formation at interfaces and diffusion processes. 1994; pp 527–548.

(41) Drillet, P.; Zermout, Z.; Bouleau, D.; Mataigne, J.; Claessens, S. Selective oxidation of high Si, Mn and Al steel grades during recrystallization annealing and steel/Zn reactivity. *La Revue de Métallurgie-CIT* **2004**, *101*, 831–837.

(42) Cavallotti, R.; Goniakowski, J.; Lazzari, R.; Jupille, J.; Koltsov, A.; Loison, D. Role of surface hydroxyl groups on zinc adsorption characteristics on $\alpha-Al_2O_3(0001)$ surfaces: first-principles study. *J. Phys. Chem. C* **2014**, *118*, 13578–13589.

(43) Cavallotti, R.; Thi Le, H.-L.; Goniakowski, J.; Lazzari, R.; Jupille, J.; Koltsov, A.; Loison, D. New routes for engineering the adhesion at $Zn/\alpha-Al_2O_3(0001)$ interface. *Phys. Chem. Chem. Phys.* **2016**, *18*, 3032–3039.

(44) Le, H.-A. T.; Goniakowski, J.; Noguera, C.; Koltsov, A.; Mataigne, J.-M. First-principles study on the effect of pure and oxidized transition-metal buffers on adhesion at the alumina/zinc interface. *J. Phys. Chem. C* **2016**, *120*, 9836–9844.

(45) Thi Le, H.-L.; Lazzari, R.; Goniakowski, J.; Cavallotti, R.; Chenot, S.; Noguera, C.; Jupille, J.; Koltsov, A.; Mataigne, J.-M. Tuning adhesion at metal/oxide interfaces by surface hydroxylation. *J. Phys. Chem. C* **2017**, *121*, 11464–11471.

(46) Le, H.-L. T.; Goniakowski, J.; Noguera, C.; Koltsov, A.; Mataigne, J.-M. Improving adhesion at the alumina/zinc interface by stainless steel buffers. *J. Phys. Chem. C* **2017**, *121*, 25143–25151.

(47) Messaykeh, M.; Goniakowski, J.; Cabailh, G.; Jupille, J.; Lazzari, R.; Lagarde, P.; Trcera, N. Chromium adsorption reveals a persistent hydroxylation of vacuum-annealed α-$Al_2O_3(0001)$. *J. Phys. Chem. C* **2019**, *123*, 29245–29254.

(48) Rodriguez, J. A.; Kuhn, M.; Hrbek, J. Interaction of silver, cesium, and zinc with alumina surfaces: thermal desorption and photoemission studies. *J. Phys. Chem.* **1996**, *100*, 18240–18248.

(49) Cavallotti, R. Effets de la terminaison de l'α-alumine sur le comportement au mouillage du zinc. Ph.D. thesis, Pierre and Marie Curie University, France, 2014.

(50) Lazzari, R.; Jupille, J.; Cavallotti, R.; Chernysheva, E.; Castilla, S.; Messaykeh, M.; Hérault, Q.; Meriggio, E. Plasmonics of supported nanoparticles reveals adhesion at the nanoscale: implications for metals on dielectrics. *ACS Applied Nano Materials* **2020**, *3*, 12157–12168.

(51) http://www.physik.de/mateck,.

(52) Campbell, C.; Valone, S. Design consideration for simple gas dosers in surface science application. *J. Vac. Sci. Technol. A* **1985**, *3*, 408–411.

(53) Renaud, G.; Villette, B.; Vilfan, I.; Bourret, A. Atomic structure of the $\alpha-Al_2O_3(0001)(\sqrt{31} \times \sqrt{31})R \pm 9°$ reconstruction. *Phys. Rev. Lett.* **1994**, *73*, 1825–1828.

(54) Guénard, P.; Renaud, G.; Barbier, A.; Gautier-Soyer, M. Determination of the α-$Al_2O_3(0001)$ surface relaxation and termination by measurements of crystal truncation rods. *Surf. Rev. Lett.* **1998**, *5*, 321.

(55) Renaud, G. Oxide surfaces and metal/oxide interfaces studied by Grazing Incidence X-Ray Scattering. *Surf. Sci. Rep.* **1998**, *32*, 1–90.

(56) Kaplan, W. D.; Mxillejans, H.; Rühle, M.; Rödel, J.; Claussen, N. N. Ca segregation to basal surfaces in

α-alumina. *J. Am. Ceram. Soc.* **1995**, *78*, 2841–2844.

(57) Lazzari, R.; Jupille, J.; Cavallotti, R.; Simonsen, I. Model-free unraveling of supported nanoparticles plasmon resonance modes. *J. Phys. Chem. C* **2014**, *118*, 7032–7048.

(58) Bedeaux, D.; Vlieger, J. *Optical Properties of Surfaces*; Imperial College Press: London, 2001.

(59) Lazzari, R.; Simonsen, I.; Jupille, J. Interfacial susceptibilities in nanoplasmonics via inversion of Fresnel coefficients. *Plasmonics* **2014**, *9*, 261–272.

(60) Lazzari, R.; Renaud, G.; Revenant, C.; Jupille, J.; Borenstzein, Y. Adhesion of growing nanoparticles at a glance: Surface differential reflectivity spectroscopy and grazing incidence small angle X-ray scattering. *Phys. Rev. B* **2009**, *79*, 125428.

(61) Simonsen, I.; Lazzari, R.; Jupille, J.; Roux, S. Numerical modelling of the optical response of supported metallic particles. *Phys. Rev. B* **2000**, *61*, 7722–7733.

(62) Lazzari, R.; Simonsen, I. `GranFilm`: a software for calculating thin-layer dielectric properties and Fresnel coefficients. *Thin Solid Films* **2002**, *419*, 124–136.

(63) Lazzari, R.; Roux, S.; Simonsen, I.; Jupille, J.; Bedeaux, D.; Vlieger, J. Multipolar optical absorptions in supported metallic particles: the case of $Ag/Al_2O_3(0001)$. *Phys. Rev. B* **2002**, *65*, 235424–1.

(64) Lazzari, R.; Jupille, J. Quantitative analysis of nanoparticle growth through plasmonics. *Nanotechnology* **2011**, *22*, 445703.

(65) `GranFilm` can be downloaded with a user guide from: http://www.insp.jussieu.fr/-Logiciels-.html.

(66) Yeh, J.; Lindau, I. Atomic subshell photoionization cross sections and assymetry parameters: $1 \leq Z \leq 300$. *At. Data Nucl. Data Tables* **1985**, *32*, 1–155.

(67) Tougaard, S. Universality classes of inelastic electron scattering cross-sections. *Surf. Interface Anal.* **1997**, *25*, 137–154.

(68) Jablonski, A. Evaluation of procedures for overlayer thickness determination from XPS intensities. *Surf. Sci.* **2019**, *688*, 14–24.

(69) Jablonski, A.; Powell, C. J. The electron attenuation length revisited. *Surf. Sci. Rep.* **2002**, *47*, 33–91.

(70) Jablonski, A.; Powell, C. J. Improved algorithm for calculating transport cross sections of electrons with energies from 50 eV to 30 keV. *Phys. Rev. B* **2007**, *76*, 085123.

(71) Jablonski, A. Photoelectron transport in the surface region of solids: universal analytical formalism for quantitative applications of electron spectroscopies. *J. Phys. D: Appl. Phys.* **2015**, *48*, 075301.

(72) Tanuma, S.; Powell, C. J.; Penn, D. R. Calculation of electron inelastic mean free paths (IMFPs) VII. Reliability of the TPP-2M IMFP predictive equation. *Surf. Interface Anal.* **2003**, *35*, 268–275.

(73) Lazzari, R. `Igor Pro Paris Photoemission Package` can be downloaded with a user guide from: http://www.insp.upmc.fr/I4P-Igor-Pro-Paris-Photoemission.html?lang=en.

(74) Ibach, H. *Physics of Surfaces and Interfaces*; Springer-Verlag Berlin Heidelberg, 2006; Vol. 10.

(75) Redhead, P. A. Thermal desorption of gases. *Vacuum* **1962**, *12*, 203–211.

(76) De Jong, A. M.; Niemantsverdriet, J. W. Themal desorption analysis: comparative test of ten commonly applied procedures. *Surf. Sci.* **1990**, *233*, 355–365.

(77) Messaykeh, M. A fundamental approach of the wetting at Zn/Cr/Al_2O_3 interface: the effect of a Cr buffer. Ph.D. thesis, Sorbonne University, France, 2018.

(78) Palik, E. D. *Handbook of Optical Constants of Solids*; Academic Press, 1985; Vol. 1-3.

(79) Sterrer, M.; Freund, H. J. Towards realistic surface science models of heterogeneous catalysts: influence of support hydroxylation and catalyst preparation method. *Catal. Lett.* **2013**, *143*, 375–385.

(80) Libuda, J.; Frank, M.; Sandell, A.; Andersson, S.; Brühwiler, P. A.; Baümer, M.; Mårtenson, N.; Freund, H. J. Interaction of rhodium with hydroxylated model substrates. *Surf. Sci.* **1997**, *384*, 106–119.

(81) Niu, C.; Shepherd, K.; Martini, D.; Tong, J.; Kelber, J.; Jennison, D. R.; Bogicevic, A. Cu interactions with α-Al_2O_3(0001): effects of surface hydroxyl groups versus dehydroxylation by Ar-ion sputtering. *Surf. Sci* **2000**, *465*, 163–176.

(82) Kelber, A.; Niu, C.; Shepherd, K.; Jennison, D. R.; Bogicevic, A. Copper wetting of α-Al_2O_3(0001): theory and experiment. *Surf. Sci.* **2000**, *446*, 76–88.

(83) Lazzari, R.; Jupille, J. Chemical reaction via hydroxyl groups at the Ti/α-Al_2O_3 interface. *Surf. Sci.* **2002**, *507-510*, 683–687.

(84) Baima, J.; Le, H. L. T.; Goniakowski, J.; Noguera, C.; Koltsov, A.; Mataigne, J.-M. Theoretical study of metal/silica interfaces: Ti, Fe, Cr and Ni on beta-cristobalite. *Phys. Chem. Chem. Phys* **2020**, *2*, 21453–21462.

(85) Vapor pressure calculator: https://www.iap.tuwien.ac.at/.

(86) Anders, A. A structure zone diagram including plasma-based deposition and ion etching. *Thin Solid Films* **2010**, *518*, 4087–4090.

(87) Depla, D.; Braeckman, B. R. Quantitative correlation between intrinsic stress and microstructure of thin films. *Thin Solid Films* **2016**, *604*, 90 – 93.

(88) NIST X-ray photoelectron spectroscopy database. https://srdata.nist.gov/xps/Default.aspx.

(89) Ley, L.; Kowalczyk, S. P.; McFeely, F. R.; Pollak, R. A.; Shirley, D. A. X-ray photoemission from zinc: evidence for extra-atomic relaxation via semilocalized excitons. *Phys. Rev. B* **1973**, *8*, 2392–2402.

(90) Kowalczyk, S. P.; Pollak, R. A.; McFeely, F. R.; Ley, L.; Shirley, D. A. $L_{2,3}M_{45}M_{45}$ Auger spectra of metallic copper and zinc: theory and experiment. *Phys. Rev. B* **1973**, *8*, 2387–2391.

(91) Schön, G. Auger and direct electron spectra in X-ray photoelectron studies of zinc, zinc oxide, gallium and gallium oxide. *J. Electron Spectrosc. Relat. Phenom.* **1973**, *2*, 75–86.

(92) Antonides, E.; Janse, E. C.; Sawatzky, G. A. LMM Auger spectra of Cu, Zn, Ga, and Ge, II. Relationship with the L_{23} photoelectron spectra via the $L_2L_3M_{45}$ Coster-Kronig process. *Phys. Rev. B* **1977**, *15*, 4596.

(93) Antonides, E.; Janse, E. C.; Sawatzky, G. A. LMM Auger spectra of Cu, Zn, Ga, and Ge. I. Transition probabilities, term splittings, and effective Coulomb interaction. *Phys. Rev. B* **1977**, *15*, 1669.

(94) Fox, J. H.; Nuttall, J. D.; Gallon, T. E. Solid state effects in the Auger spectrum of zinc and oxidized zinc. *Surf. Sci.* **1977**, *63*, 390–402.

(95) Kourouklis, H.; Nix, R. The uptake and characterisation of zinc on low index silver and copper surfaces. *Surf. Sci.* **1994**, *314*, 201 – 211.

(96) Rodriguez, J. A.; Kuhn, M. Interaction of zinc with transition-metal surfaces: electronic and chemical perturbations induced by bimetallic bonding. *J. Phys. Chem.* **1996**, *100*, 381–389.

(97) Rodriguez, J. A. Physical and chemical properties of bimetallic surfaces. *Surf. Sci. Rep.* **1996**, *24*, 223 – 287.

(98) Jeroro, E.; Lebarbier, V.; Datye, A.; Wang, Y.; Vohs, J. M. Interaction of CO with surface PdZn alloys. *Surf. Sci.* **2007**, *601*, 5546 – 5554.

(99) Ho, C. S.; Martono, E.; Banerjee, S.; Roszell, J.; Vohs, J.; Koel, B. E. Alloy formation and chemisorption at Zn/Pt(111) bimetallic surfaces using alkali : ISS, XPD, and TPD. *J. Phys. Chem. A* **2013**, *117*, 11684–11694.

(100) Wagner, T.; Fu, Q.; Winde, C.; Tsukimoto, S.; Phillipp, F. A comparative study of the growth of Cr on (110)TiO_2 rutile, (0001)α-Al_2O_3 and (100)$SrTiO_3$ surfaces. *Interface Sci.* **2004**, *12*, 117–126.

(101) http://www.webelements.com.

(102) Jeffers, G.; Dubson, M. A.; Duxbury, P. M. Island to percolation transition during growth of metal films. *J. Appl. Phys.* **1994**, *75*, 5016–5020.

(103) Zhao, G.; Jeong, E.; Choi, E. A.; Yu, S. M.; Bae, J.-S.; Lee, A.-G.; Han, S. Z.; Lee, G. H.; Yun, J. Strategy for improving Ag wetting on oxides: Coalescence dynamics versus nucleation density. *Appl. Surf. Sci.* **2020**, *510*, 145515.

(104) Haarmans, M.; Bedeaux, D. Optical properties of thin films up to second order in the thickness. *Thin Solid Films* **1995**, *258*, 213–223.

(105) Nash, D. J.; Sambles, J. R. Surface plasmon-polariton study of the optical dielectric function of zinc. *J. Mod. Opt.* **1998**, *45*, 2585–2596.

For Table of Contents Use Only

Title: An *In Situ* and Real Time Plasmonic Approach of Seed/Adhesion Layers: Chromium Buffer Effect at the Zinc/Alumina Interface

Authors: Maya Messaykeh, Stéphane Chenot, Pascal David, Gregory Cabailh, Jacques Jupille, Alexey Koltsov, Rémi Lazzari

TOC Graphic

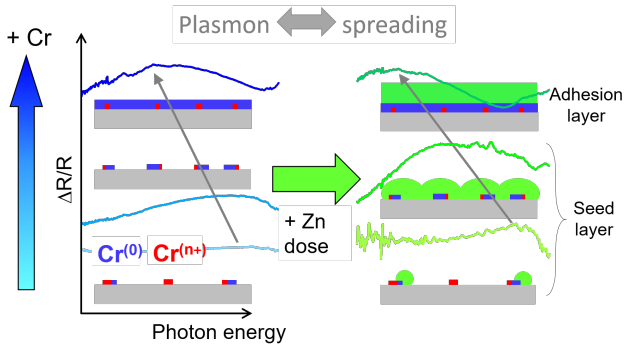

Outline of Cr buffer effect on Zn/Al_2O_3 growth as derived from plasmonics.